Final version June 21, 2024
Typeset using LaTeX default style in AASTeX631

On the Detectability of Emission from Exoplanet Outflows

Riley Rosener,[1] Michael Zhang,[1] and Jacob Bean[1]

[1] *University of Chicago*
5640 S Ellis Ave, Ste 599
Chicago, IL 60637, USA

ABSTRACT

Exoplanets close to their host stars experience high amounts of irradiation, causing drastic atmospheric escape that can be measured as a gas outflow from the planet using certain chemical tracers. To date, exoplanet atmospheric escape has thus far only been probed using transmission spectroscopy to measure line absorption. While it is theoretically possible to measure outflows via emission spectroscopy, the observability of these signatures may limit the practical application of this method. In this work, we investigate different strategies of observing atmospheric outflow emission, finding that Hα and He* consistently give the highest signal-to-noise ratio (SNR) across all planets tested. We consider a variety of exoplanets with confirmed detections of the 10833$\mathring{A}$ metastable helium absorption line and other outflow tracers. We use the updated and improved PyTPCI (The-PLUTO-CLOUDY Interface) software and wrapper with enhanced stability and usability to run combined 1D photochemistry, spectrum synthesis, and hydrodynamics simulations of our chosen exoplanet systems. Using these results and information about the observational facilities that are most sensitive to each diagnostic, we calculate the resultant signal-to-noise ratio, eclipse depth, optical depth, bremsstrahlung flux, and theoretical mass loss rates for our target systems. Ultimately, we find that these signals will not be large enough to detect and distinguish during the secondary eclipse using existing facilities in less than 5 transits. We find a maximum predicted signal-to-noise ratio of 2.4 from the hot Jupiter HD 189733b at 10$\times$ solar metallicity in the He* line. For future observational campaigns, our work suggests focusing on bright, well-characterized systems like hot Jupiters HD 189733b and HD 209458b, so that any potential emission signals are maximized. Although these emissions are not currently detectable with Keck and HST, they may be within reach of the next generation of extremely large telescopes.

1. INTRODUCTION

The study of escaping exoplanet atmospheres is only 20 years old (Vidal-Madjar et al. 2003), and yet the development of novel approaches to atmospheric modeling and observing is rapidly advancing the field. Short-period exoplanets experiencing strong irradiation at high-energy wavelengths will gradually have their atmospheres stripped away via photoevaporation, although the specific mechanisms and timescales of this process are still controversial. In order to better characterize the properties of this hot gas outflow, we investigate the observability of emission signatures from the escaping atmosphere, which encode information about the temperature and species density of the upper layers of the atmosphere. In this work, we calculate the observability using the spectrum synthesis, photochemistry, and hydrodynamics simulation TPCI (The PLUTO-CLOUDY Interface) to model the planetary gas outflow.

One-dimensional simulations cannot model important three-dimensional phenomena such as winds resulting from large dayside-nightside temperature gradients or aerosols like clouds and hazes (Harada et al. 2021; Malsky et al. 2024). However, despite the fact that photoevaporative mass loss ultimately requires description via 3D models, we can still use 1D models like TPCI to roughly approximate reality. Significantly, the lower dimension of TPCI allows for rapid evaluation and therefore more thorough modeling of energy levels and chemical species than is possible for 3D models (Zhang et al. 2022b).

For our observables, we examine emission in Hα and metastable helium, as well as bremsstrahlung emissions, and additionally calculate values commonly used to assess observability, such as eclipse depth and the optical depth in Hα. Metastable helium (He*) is an excellent probe into planetary atmospheres that are being strongly irradiated by X-ray and UV wavelengths, causing escape of the upper atmosphere (Oklopčić & Hirata 2018). Strong metastable helium

absorption in transmission spectra was first predicted by Seager & Sasselov (2000) in their analysis of gas giant HD 209458b, though most successful observations with this line have been undertaken recently (e.g. Zhang et al. 2022b; Spake et al. 2018; Nortmann et al. 2018). Due to the improving success of detecting and interpreting this line, we select it as one of our potential observables.

We choose to examine the emission of Hα due to the abundance of hydrogen in some exoplanet atmospheres, especially in the close-in planets we are able to observe transiting. Hα has been detected in exoplanet atmospheres such as HD 1897333b and HD 209458b (Jensen et al. 2012; Casasayas-Barris, N. et al. 2018). The sensitive nature of the $n = 2$ state of hydrogen acts as a precise probe into the temperature profile of these hydrogen-rich escaping atmospheres (Christie et al. 2013). Additionally, the absorption of near-ultraviolet emission that forms the Hα line points towards a potential avenue of hydrodynamic escape in ultra-hot exoplanet atmospheres. (García Muñoz & Schneider 2019). We also examine bremsstrahlung radio emission, which is theoretically produced by the self-interaction of the abundant free electrons in the atmospheric outflow plasma.

The vast majority of exoplanet upper atmosphere characterization has been performed with transmission spectroscopy, measuring the expected changes in stellar flux from the light transmitted through the limb of the planet's extended atmosphere (Winn 2014). Thus far, exoplanet outflows have only been probed with transmission spectroscopy.

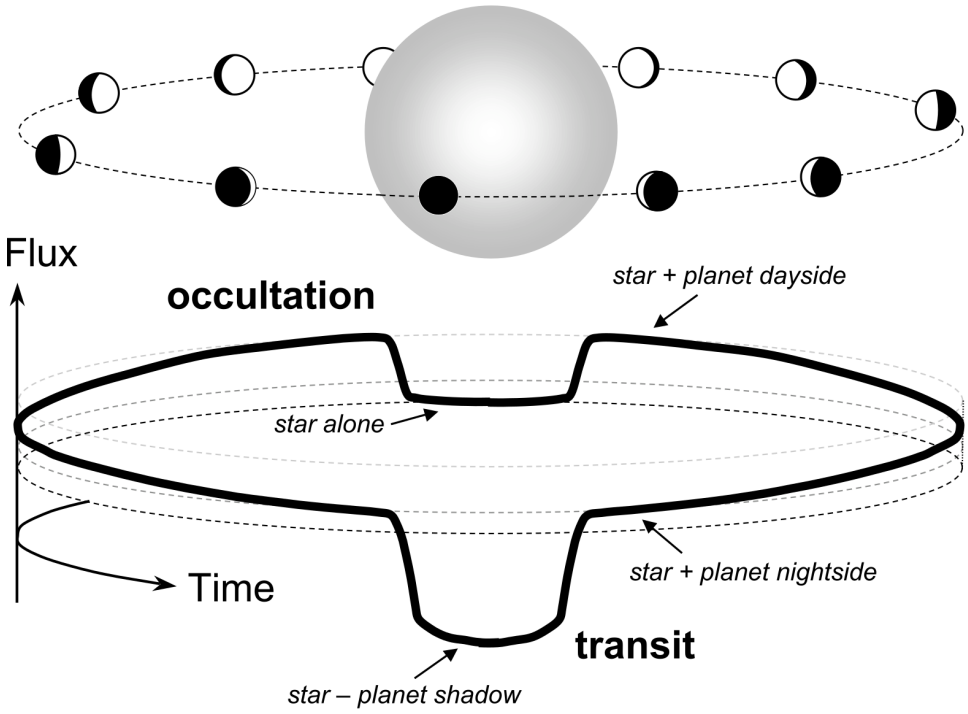

Figure 1: A diagram of exoplanet transits and occultations, Fig. 1 of Winn (2014). Our region of interest is the secondary eclipse, labeled here as "occultation".

However, little research has been done to examine the detectability of planetary outflow emission signatures during the secondary eclipse, when an exoplanet passes behind its host star (see Figure 1). The measured flux during that secondary eclipse (or occultation) would be less than the baseline flux, since light from the occulted planet's dayside is blocked by the star. Accordingly, high-quality baseline flux measurements before and after the secondary eclipse would provide the emitted flux from the planet. This flux would normally be composed of thermal radiation and negligible amounts of reflected stellar light (Winn 2014). However, in the case of exoplanets actively losing their atmosphere, their energetic outflows may emit significant flux. In this thesis, we investigate the overall planetary emission spectrum from the outflow predicted by PyTPCI, and briefly examine the cases of bremsstrahlung emitted by the plasma.

This thesis is organized as follows — in Section 2, we describe the simulation of PyTPCI and its components. In Section 3 we discuss the different systems we modeled. We present our main observability calculations in Section 4.

In Section 5, we calculate the optical depths. In Section 6, we present our bremsstrahlung calculations, and in Section 7 we describe our mass loss calculations. Finally, in Section 8 we summarize our results and in Section 9 we discuss our findings.

2. THE TPCI SIMULATION

TPCI (The PLUTO-CLOUDY Interface) is a code interface between the general magneto-hydrodynamics code PLUTO (Mignone et al. 2007) and the gas microphysics code CLOUDY (Chatzikos et al. 2023), originally developed and released in Salz et al. (2015) in order to simulate planetary outflows from strong stellar irradiation in 1D. PLUTO and CLOUDY are called iteratively, one after the other, tracing the evolution of the model exoplanet's atmosphere as it becomes irradiated, until TPCI reaches a steady-state solution.

We create a one-dimensional simulation domain, ranging from 1 to 15 planetary radii above the planet's surface. First, PLUTO solves the Navier-Stokes fluid dynamics equations and enforces conservation laws, and outputs density, pressure, and velocity distributions for the gas as functions of radius, which can be used to estimate the temperature profile. These are then fed into CLOUDY, which produces a radiative heating distribution with values for heating and cooling across the domain, as well as detailed information on radiation transfer and the populations and properties of many chemical species. This heating distribution is put back into PLUTO, updating the hydrodynamics and stepping forward in time. This iterative loop is repeated until the system reaches a steady state. Ultimately, CLOUDY outputs a continuum spectrum of the radiation emitted by the outflow, with which we can calculate detectability measures like the signal-to-noise ratio, and some other information which can be used to estimate optical depth.

2.1. *PyTPCI*

What we refer to as "PyTPCI" is the final custom version of TPCI used to run our simulations, which features a new Python wrapper that does not requiring direct editing of configuration files and recently updated versions of PLUTO and CLOUDY. We also incorporate a variety of bug fixes to increase stability, as described in Section 2.3, but key among them is setting a higher kinetic temperature floor and adaptively setting the shear viscosity constant. The repository is publicly listed on GitHub[1], and we plan to further optimize this code for future use.

2.2. *Simulation Setup and Inputs*

Much thought and experimentation was put into the specific combinations of parameters used while running PyTPCI. We fine-tuned parameters used to initialize our simulation in order to balance numerical stability and accuracy. The full set of input parameters is shown in Table 1. We describe our parameter selection process below, which we then used to model a variety of different exoplanets.

2.2.1. *Planet Parameters*

For a given system, the planet parameters such as planet mass, radius, and semimajor axis were taken from the most recent literature. The initial temperature profile of each planet being simulated is modeled as isothermal, with the initial temperature set to its equilibrium temperature. A fixed planetary albedo was not assumed, but rather each equilibrium temperature was taken from the NASA Exoplanet Archive[2], where sources vary on their assumptions and modelling methodologies. The metallicity used for each planet was determined on a case-by-case basis, with a run at 1× solar metallicity labeled as "1Z", one at 10× solar metallicity labeled as "10Z", and so forth. See Table 1 for the different metallicities used.

2.2.2. *Stellar Parameters and Spectra*

Chemistry caused by high-energy X-rays and UV radiation significantly impacts the composition of an exoplanet's upper atmosphere and must be incorporated during outflow modelling, especially in our context of simulating gas giants' escaping atmospheres. The secondary electron cascade that dominates most X-ray photochemical reactions is included by default in all CLOUDY photoionization simulations (Locci et al. 2022; Chatzikos et al. 2023). X-rays and extreme UV radiation in particular drive photoevaporation, the key phenomenon we intend to study, and so it is necessary that we have precise and well-constrained stellar spectra at these energies.

[1] https://github.com/ideasrule/pytpci

[2] https://exoplanetarchive.ipac.caltech.edu/

Table 1: PyTPCI Input Parameters

System	Star Temperature (K)	$F_{Ly\alpha}$	F_X	Distance (pc)	Semimajor Axis (AU)	Mass ($M_\oplus$)	Radius ($R_\oplus$)	T_{eq} (K)	Metallicity ($[M/H]_\odot$)
HD 209458b	6026	20.94	0.57	48.30	0.04723	219	15.1	1320	0, 1
TOI-560b	4500	15	19	31.57	0.0596	11	2.9	740	0, 100
WASP-69b	4715	10	8.4	49.96	0.045	92	12.4	963	0, 10
WASP-107b	4400	29.3	8.15	64.74	0.0553	38	10.4	770	0
HD 189733b	5012	15	7.7	19.76	0.03126	371	12.54	1209	0, 10
TOI-1430b	5037	23	8	41.17	0.072	7	2.04	800	0, 100

NOTE—Fluxes given at 1AU from host system in CGS units.

In order to properly simulate the stellar spectrum of the host star, we build off of Wood et al. (2005), who showed correlations between Lyα and X-ray flux in stars of certain spectral types. In particular, we use the scaling relations for K-dwarfs in Linsky et al. (2020) in order to estimate stellar Lyα flux for a number of our systems that do not have well-characterized host stars.

Our construction of the input stellar spectra follows the procedure laid out in Salz et al. (2016). This requires input parameters of corona temperature and density, total X-ray flux, Lyα flux, distance from Earth, stellar effective temperature, stellar radius, and stellar luminosity. The resultant spectrum consists of:

1. A 0–100$\mathring{A}$ X-ray model from the CHIANTI astrophysical plasma database (Dere et al. 1997; Del Zanna et al. 2021).
2. A Lyα emission line modeled by a Gaussian of FWHM 9.4$\mathring{A}$.
3. A 100–912$\mathring{A}$ EUV spectrum from solar measurements, scaled by the input Lyα flux (Woods & Rottman 2002).
4. A blackbody spectrum up to 50,000$\mathring{A}$ from the PHOENIX high-resolution synthetic stellar spectra database (Husser et al. 2013).

A similar approach is also taken by Locci et al. (2022), incorporating an X-ray-dependent Lyα profile and building off PHOENIX spectra, though their spectra in the X-ray regime instead uses Raymond-Smith hot plasma models (Raymond & Smith 1977).

2.2.3. *CLOUDY Setup*

CLOUDY is purely 1D, simulating a gas cloud via a series of shells that extend from an inner radius to an outer radius, with a radiation source — the host star — at the center. However, since our inner radius (the semimajor axis) is much larger than the thickness of the gas cloud (14 planetary radii), the geometry is effectively plane-parallel. The CLOUDY code uses "depths" instead of radii, which is defined to be the distance from the illuminated front of the gas cloud to another point inside the cloud. We use the command `double optical depths` in order to properly take the 1D geometry in account, so that emitted radiation cannot escape through the simulated planet's "ground" at the edge of the simulation domain.

By default, the illumination angle of the gas cloud simulated by CLOUDY is 0°, where radiation would be hitting the substellar point of our 1D planet. However, Johnstone et al. (2018) showed that adopting an illumination angle of 66° is a good approximation for the global average of calculated parameter profiles. We adopt this methodology for our simulations.

CLOUDY can only solve for positive velocity outflows, and not negative velocity inflows. This behavior requires further tuning in order to implement a more numerically-stable solution. In order to fix this, we simply convert negative velocities from PLUTO into positive when fed into CLOUDY, since all velocities ought to be positive when the outflow is in equilibrium. Due to computational limitations, we do not model molecules. In order to increase

stability and to allow the simulation to converge, advection in CLOUDY is only enabled once PyTPCI has reached approximately 10% of its total runtime.

As input, CLOUDY requires a spectral energy distribution of the incident radiation field from the source, which in our case is the stellar spectrum at 1 AU specified using CLOUDY's `intensity` case. The mean molecular weight μ of the entire gas cloud is computed as a function of metallicity. As this is a driving indicator of chemical composition, it is allowed to vary as a function of depth. Runs with nonzero metallicity include elements with solar abundances greater than 10^{-5}. CLOUDY outputs are highly configurable, but we particularly want the radiation emitted at each wavelength, and as functions of depth, the temperature and the number densities and ionization fractions of various chemical species. As an output from CLOUDY, we record radiation emitted at each wavelength. As functions of depth, we also record the temperature, and the number densities and ionization fractions of various chemical species.

2.2.4. *PLUTO Setup*

Through the previous results of Salz et al. (2016) and trial-and-error, we discovered the ideal combination of hydrodynamical simulation reconstruction methods, time stepping methods, and solvers for stability. As in Salz et al. (2016), we create a 1D grid in Cartesian coordinates in a domain extending from 1 to 15 planetary radii, with finer, uniform spacing at lower radii, and stretched spacing at higher radii. PLUTO naturally implements methods to ensure points near boundary domains behave well. We run all simulations in the standard classical hydrodynamic `HD` mode, solving the Navier-Stokes equations.

For simulation parameters, we use a 3rd-order TVD Runge Kutta `RK3` time stepping combined with a `WENO3` reconstruction, giving a 3rd-order spatial integration. It must be noted that we use the finite volume version of the code, in which fluid parcels are averaged over a cell as if binned inside a histogram (Diemer 2022, Ch. 6.5). In this mode, computed fluxes retain only a 2nd-order global accuracy. For flux computations, we choose the `hllc` Riemann solver, which is more accurate and stable than the simple `tvdlf` solver used in previous publications (Mignone et al. 2007).

We also include the effects of thermal conduction and viscosity to further stabilize the simulation, with both using the super-time-stepping method `STS`. The thermal conduction coefficient is set to the default. However, we set the shear viscosity coefficient according to the density at the given grid point, in order to keep the grid-scale Reynolds number $\mathcal{O}(1)$.

$$Re \equiv \frac{U\Delta}{\nu} \sim \mathcal{O}(1) \tag{1}$$

It is worth noting that the PLUTO code and documentation labels this constant as the kinematic viscosity ν_1, but the parameter is actually the dynamic viscosity $\mu = \rho\nu$. More information on these choices will be provided in Subsection 2.3.

2.3. *Troubleshooting and Methodology*

The original version of TPCI was rather unstable and prone to crash during various points in a given simulation. As a result, getting a simulation to run for any given planet required some trial-and-error.

One common behavior exhibited by TPCI was sharp temperature spikes in the CLOUDY temperature outputs of order $\sim 10^4 - 10^6$ K, which caused drastic discontinuities and crashed CLOUDY. This transient phenomenon was the result of suddenly exposing an isothermal, non-evaporating atmosphere to high-energy radiation. Accordingly, we thoroughly investigated the choice of time stepping method, reconstruction, and Riemann solver. Initial tests using the more simple and stable `RK2` time stepping with `LINEAR` reconstruction showed the same issues, as did `RK3`, even with viscosity and thermal conduction disabled. Other time stepping methods experience less numerical dissipation, but their additional technical difficulties were not worth minor improvements in accuracy. Different reconstruction methods such as `PARABOLIC` and `LimO3` were not tested, due to the greater constraints they experience with setup geometry and the CFL criterion.

We suspected that the `tvdlf` solver was the cause of this phenomenon, though we obtained identical solutions for `tvdlf` and `hllc` in the final form of PyTPCI. However, one change that proved effective was altering the shear viscosity constant ν_1 at each grid point as shown in Equation 1, instead of setting it to be a global constant. Setting the characteristic velocity $U \sim 10$ km/s and the grid spacing $\Delta \sim 0.0002$ was usually stable and prevented CLOUDY from crashing due to the time stepping being too small, although sometimes Δ was halved for smaller mini-Neptunes like TOI-560b and TOI-1430b.

Another significant behavior exhibited by both TPCI and PyTPCI is the tendency for stable sound waves to form, particularly in all simulations of HD 189733b and some of TOI-560b. These are numerical artifacts resulting from how

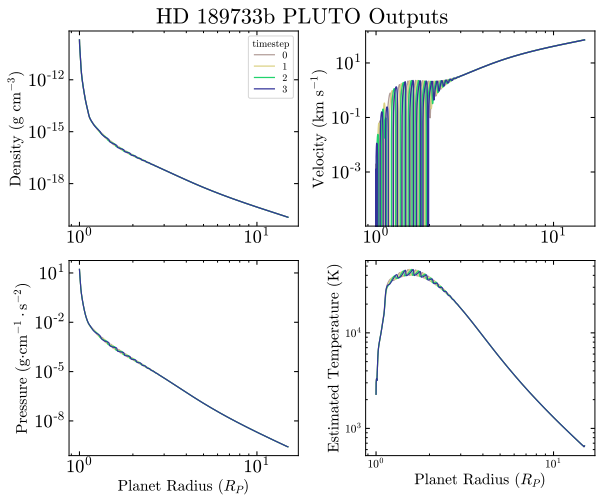

(a) Sound waves before damping.

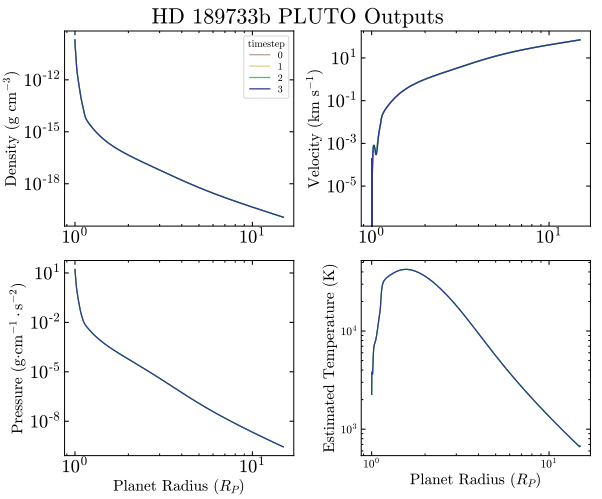

(b) Sound waves after damping.

Figure 2: HD 189733b with and without sound waves. The stable sound waves are particularly visible in the velocity, but note the small perturbations in density and pressure near $R_P = 1$. The waves were eliminated by setting the time step equal to the wave period. There are now few differences between successive iterations.

the initial simulation conditions are implemented. In general, the formation of nonphysical sound waves is a common problem in many hydrodynamic atmosphere simulations. These waves normally do not constructively interfere and increase in magnitude, but they do blur out data and cause drastic swings in velocity. We were able to measure the wave period and speed, and positively confirm that the waves were traveling at the speed of sound. By setting the time step to the wave's period and fixing it, we successfully froze the waves in place, as shown in Figure 2.

Occasionally, longer wavelength and period propagating waves appear, such as in the high-metallicity runs of TOI-1430b and WASP-69b. We do not have a recommended solution for these waves, besides taking a data file where the perturbations are minimal. Increasing the metallicity of any given system does increase numerical instability, which will ultimately require more creative solutions to ensure proper functioning.

Finally, when experiencing temperature spikes and discontinuities, CLOUDY would sometimes drop below its default kinetic temperature of 2.8 K. Forcing the kinetic temperature floor to be 28 K instead fixes this unusual behavior.

A successful PyTPCI simulation takes approximately 48 hours wall time to converge on an Intel Core i9 Processor (32×5.5 GHz) with 64 GB RAM, though it takes much longer for tenuously-stable cases like HD 189733b.

3. PYTPCI RUNS

Multiple iterations of PyTPCI were run for each planetary system, in order to test the code. The final versions shown are the most recent runs, some of which were at zero metallicity with only hydrogen and helium present (HD 209458b, WASP-69b, and WASP-107b). These were done in order to maximize speed and stability and to compare results with Salz et al. (2016), under the assumption that differences between 0Z and 1Z would be minimal. Other runs had higher-than-solar metallicities with more elements present (TOI-560b, TOI-1430b, and HD 189733b).

Each emission spectrum plot displays wavelength versus wavelength-dependent flux, and includes the integrated flux calculated for our labelled spectral lines of focus: Hα, and metastable helium. Refer to Table 1 to see the values of all system parameters used to run PyTPCI for each exoplanet.

3.1. *HD 209458b*

HD 209458b was the first exoplanet ever found by the transit method, observed by Charbonneau et al. (2000) and confirmed by prior radial velocity measurements of the system. It is a classic "hot Jupiter", a massive, short-period gas giant that experiences significant irradiation from its host star, and is the most easily-detected type of exoplanet. It also hosts the first exoplanet atmosphere detected and has frequently been the target of atmospheric studies, such as the collection of a JWST transmission spectrum suggesting the presence of H_2O and CO_2 (Xue et al. 2024). There

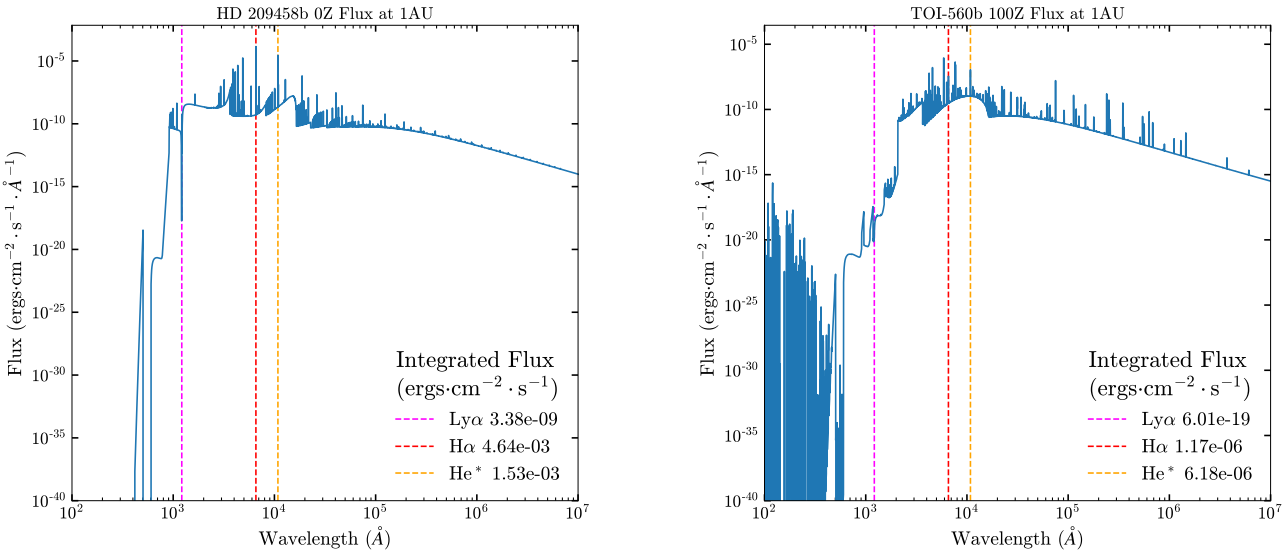

Figure 3: PyTPCI emission spectra of HD 209458b and TOI-560b. HD 209458b only shows the continuum from hydrogen and helium, with the prominent line at 505$\mathring{A}$ being from neutral helium. At 100× solar metallicity, TOI-560b shows a much larger amount of short wavelength emission lines, including sodium and potassium lines in the optical.

also exists a debate over whether Na D absorption was detected in the its atmosphere (e.g. Charbonneau et al. 2002; Snellen et al. 2008; Casasayas-Barris et al. 2021).

We initially ran HD 209458b with zero metallicity in order to test computational stability, and it was relatively well-behaved in PyTPCI. See Figure 3 for its emission spectrum. Due to its host star's hot surface temperature, it is as predicted quite bright. We later ran the system with 1Z metallicity, which did not alter the Hα and He* SNRs, but did triple the predicted helium absorption and equivalent width. However, this result should be considered dubious, since the 0Z metallicity simulation is much more consistent with the observed equivalent width, as shown in Table 3. Its resultant spectrum is shown in the left panel of Figure 3.

3.2. *TOI-560b*

Two transiting exoplanets were discovered in the HD 73583 system by TESS (Barragán et al. 2022), with both being "mini-Neptunes". This is a type of planet intermediate in size between Earth and Neptune of 1–4 $R_\oplus$, particularly having bulk densities indicating a solid core and substantial gaseous envelope (Zhang et al. 2022b). This class of exoplanets is increasingly studied as the key to understanding mass loss in young planets and the creation of the radius gap. As a nearby exoplanet orbiting a young, bright star, TOI-560b is an excellent target to study mass loss, with a confirmed detection of metastable helium absorption (Zhang et al. 2022b).

Following the work of Zhang et al. (2022b), we simulated TOI-560b with super-solar metallicity. It was relatively simple to run PyTPCI models for this system, although it did display some sound waves in the 100Z runs and not the 0Z runs. Our predicted peak temperature and maximum wind speed are both notably smaller than the initial calculations from Barragán et al. (2022), which suggest a peak temperature near 6,500 K and a wind velocity of 30 km/s, compared to our results of 4,800 K and 11 km/s. The spectrum is shown in the right panel of Figure 3.

3.3. *WASP-69b*

WASP-69b is a Saturn-like exoplanet orbiting an active K-dwarf with helium absorption and a potential minor gas tail. The gas tail shows an atmosphere with similar helium layer equivalent height as HD 189733b (Nortmann et al. 2018). However, this gas tail was not detected by Vissapragada et al. (2020), utilizing a new metastable helium ultranarrowband filter. Comprehensive 3D simulations by Wang & Dai (2021) support their conclusion, emphasizing the role of EUV photons in helium photoevaporation.

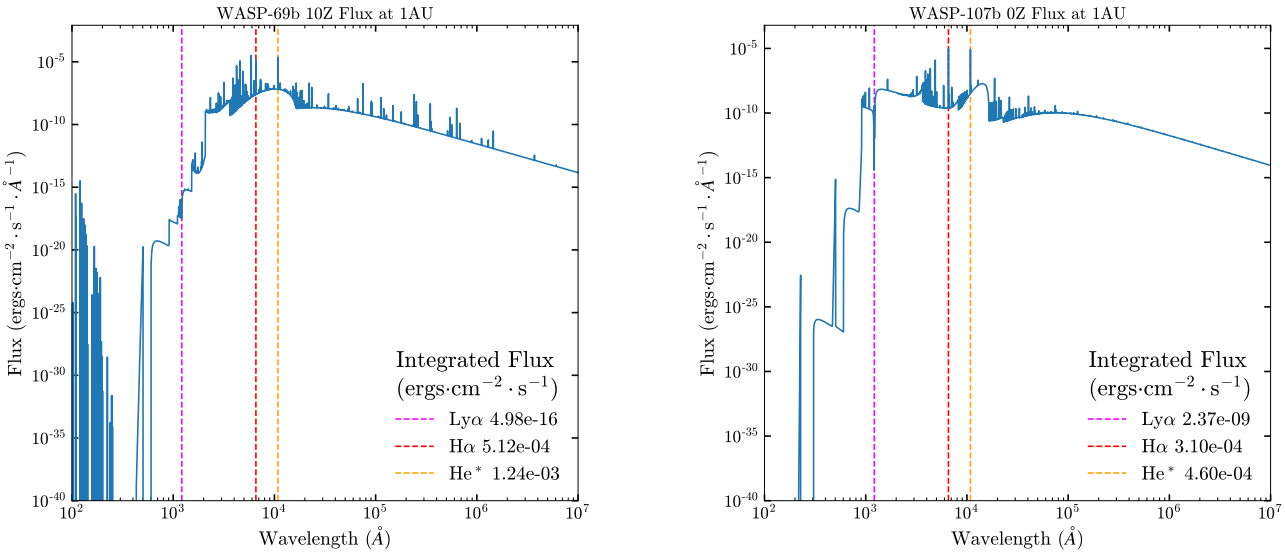

Figure 4: PyTPCI emission spectra of WASP-69b and WASP-107b. At 10× solar metallicity, WASP-69b shows some short wavelength metal emission lines. WASP-107b only shows the continuum from hydrogen and helium, and yet the dynamic structure of its outflow is still unusual.

WASP-69b behaved well in simulations, run with both 0Z and 10Z metallicity. Both simulations showed a much larger predicted helium equivalent width of 29m$\mathring{A}$ than has been previously observed and measured for WASP-69b, with a width of 76m$\mathring{A}$ for 0Z and 245m$\mathring{A}$ for 10Z (see Table 3). The 0Z model was much closer to the observed value than the 10Z model, which is shown in the left panel of Figure 4. WASP-69b is not known to have a particularly extended atmosphere, so this unexpected result of metallicity increasing equivalent width merits further consideration.

3.4. *WASP-107b*

WASP-107b is an low-density Jupiter-mass exoplanet, sometimes called a "warm Saturn" or a "sub-Neptune". A strong metastable helium absorption line has been observed and confirmed in its transmission spectrum, indicating an unusually extended atmosphere (with large atmospheric scale height) (Spake et al. 2018) and quite possibly an extended tail of helium contributing to the blue-ward asymmetry of the absorption profile (Allart, R. et al. 2019; Kirk et al. 2020). It has been a popular target for examining the complexities of atmospheric escape.

We are not fully able to capture the unique transport dynamics of WASP-107b due to PyTPCI being a 1D simulation. Nevertheless, it performed well with this system, converging quite quickly compared to the other simulations. We predicted an equivalent width of 509m$\mathring{A}$, which is much larger than the 100m$\mathring{A}$ that has been previously measured for the system (see Table 3). Notable XUV flux from the outflow was not predicted by PyTPCI, so the ultimate cause of this result is unknown. However, the effects of a radial planetary wind on an extended atmosphere has been modeled for similar exoplanet HAT-P-32b, indicating that further investigation is needed (Czesla, S. et al. 2022).

3.5. *HD 189733b*

HD 189733b is the other archetypal hot Jupiter besides HD 209458b, and remains one of the best studied exoplanet systems to date. Metastable helium absorption was detected by Salz, M. et al. (2018), fitting with the predictions of Oklopčić (2019) that K-dwarfs would be an ideal host star for populating the metastable helium state. Nevertheless, Zhang et al. (2022a) demonstrated the need to improve our understanding of both high-energy stellar irradiation and the 3D atmosphere in order to make more conclusive statements about this system and to further determine whether its production of neutral hydrogen is dominated by recombination or other physical processes (Lampón et al. 2021).

Other 1D hydrodynamic modeling indicates a very compact and hot atmosphere, with a low mean molecular mass (Lampón et al. 2021). Our model of HD 189733b at 10Z metallicity indeed predicts a very hot atmosphere with a

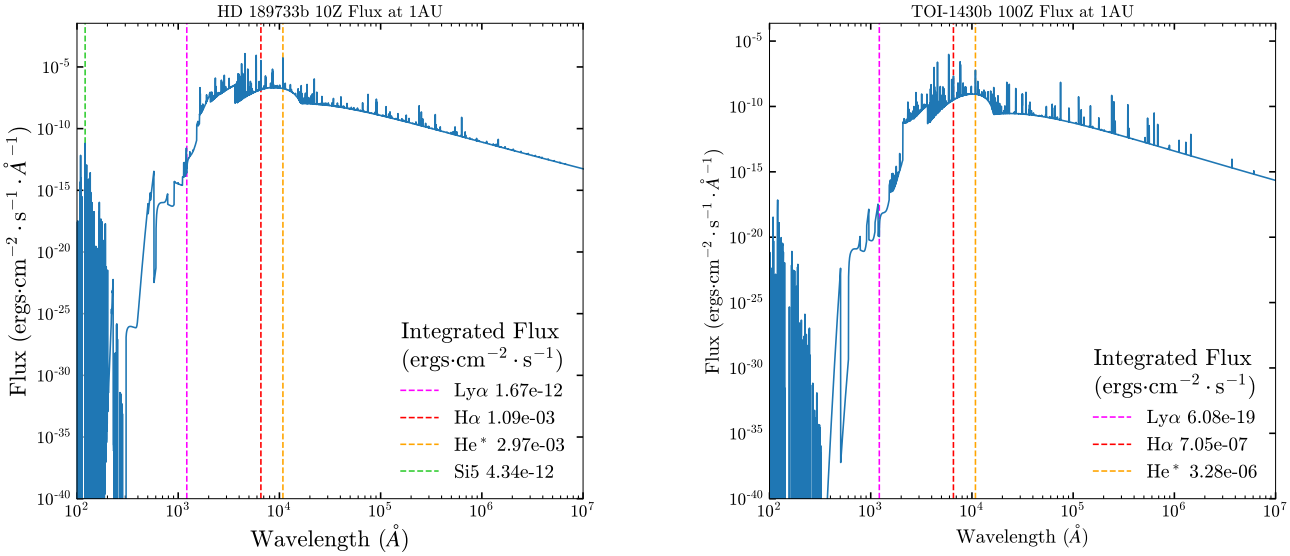

Figure 5: High metallicity spectra with prominent short-wavelength metal lines. Exact line identification is not possible due to the poor spectral resolution of PyTPCI in this regime, however a line tentatively identified as Si5+Na11 is marked for HD 189733b on the left. Prominent X-ray emission is also present, though not shown in these plots.

temperature curve peak around 10,300 K (see Table 3), and a very fast 70 km/s planetary wind outflow (see Table 4). This is shown in the left panel of Figure 5.

3.6. *TOI-1430b*

In order to fully explain the "radius gap" distinguishing smaller and denser super-Earths from mini-Neptunes, it is necessary to fully characterize the mass loss of young mini-Neptunes. One young mini-Neptune being studied for this purpose is TOI-1430b, a similar planet to TOI-560b, which is a recently-discovered TESS exoplanet orbiting a K-dwarf that has had a confirmed detection of the metastable helium absorption line (Zhang et al. 2023).

Simulations of TOI-1430b at 0Z and 100Z ran smoothly, predicting minimal emissions from this relatively small, cool planet, as consistent with prior observation. Its emission spectrum is shown in the right panel of Figure 5. Accurate mass loss rates of mini-Neptunes remain uniquely elusive, though our results are quite close to those of Zhang et al. (2023).

4. OBSERVABILITY CALCULATIONS

With the resultant PyTPCI data, we performed standard astrophysical statistics calculations to find the signal-to-noise ratio and eclipse depth in our chosen spectral lines Hα and He*. Our main data source is the `continuum` files produced by CLOUDY, which produces the planetary emission spectrum as a function of wavelength. These data include the reflected and transmitted radiation and the dominant spectral lines in that wavelength bin.

4.1. *SNR and Eclipse Depth*

In order to calculate the signal-to-noise ratio, we model the number of photons received as a Poisson distribution, and take advantage of the fact that the Poisson distribution's expectation value (mean) N is equal to its variance $\sigma^2(N)$. To denote that we are only estimating the total amount of photons received, we write this as $\hat{N}$ and $\sigma^2(\hat{N})$, where the standard deviation is simply the square root of the variance, $\sigma(\hat{N})$.

The total amount of photons received is the sum of the photons received from the background and from the source. We make the traditional astrophysical approximation that the amount of photons received from the star (the background) is much greater than the amount received from the planet (the source), so that $\hat{N} \approx N_{star}$. Accordingly, we show via linearity the variance of the total photons received as:

$$\sigma^2(\hat{N}) = \sigma^2(N_{\text{planet}}) + \sigma^2(N_{\text{star}}) \approx N_{\text{planet}} + N_{\text{star}} \approx N_{\text{star}} \tag{2}$$

Naturally, the number of photons received from the planet is the difference between the total measured flux and the stellar flux.

$$N_{\text{planet}} = \hat{N} - N_{\text{star}} \tag{3}$$

However, via uncertainty propagation, we gain an extra factor of $\sqrt{2}$ in the error from comparing the flux in-transit and out-of-transit.

$$\sigma(N_{\text{planet}}) = \sqrt{\sigma^2(\hat{N}) + \sigma^2(N_{\text{star}})} \approx \sqrt{2}\sigma(N_{\text{star}}) \approx \sqrt{2 \cdot N_{\text{star}}} \tag{4}$$

The signal-to-noise ratio is defined as a distribution's expectation value divided by its standard deviation. Thus, we estimate the SNR for a planetary emission signal as:

$$SNR = \frac{N_{\text{planet}}}{\sigma(N_{\text{planet}})} = \frac{N_{\text{planet}}}{\sqrt{\sigma^2(\hat{N}) + \sigma^2(N_{\text{star}})}} \approx \frac{N_{\text{planet}}}{\sqrt{2 \cdot N_{\text{star}}}} \tag{5}$$

In each case, the number of photons measured by the instrument is estimated as a function of the spectral flux density, mirror area, and time. We take the eclipse duration as 2 hours, and determine throughput and mirror specifications depending on the spectral line (as discussed in Section 4.2). The throughput is defined as the ratio of the number of photons measured and the true number of photons expected to enter an optical system, and is determined for a given combination of telescope, instrument, filter, and spectral line. Since the spectral flux density is a wavelength-dependent quantity in units of ergs·s^{-1}·cm^{-2}·cm^{-1}, we must include the additional factor of $\Delta\lambda$, the bin size. We include a proper distance ratio, since PyTPCI outputs spectral flux at the planet's surface, and convert between units of energy and photons. We find the total amount of photons in a wavelength band by summing over each wavelength bin i.

$$N_\lambda = F_\lambda \cdot \Delta\lambda \cdot A_{\text{mirror}} \cdot T_{\text{dur}} \cdot \left(\frac{R_p}{d}\right)^2 \cdot \frac{\lambda}{hc} \tag{6}$$

$$N = \sum_i N_{\lambda_i} \tag{7}$$

We calculate the secondary eclipse depth as the ratio between the planet and star fluxes at their surfaces, and multiply it by the squared planet-star radius ratio, taking the maximum value in each wavelength band as our final eclipse depth (Perryman 2018, Eq. 6.157).

$$\delta_\lambda \approx \left(\frac{R_p}{R_s}\right)^2 \cdot \max\left[\frac{F_{p,\lambda}}{F_{s,\lambda}}\right] \tag{8}$$

We take the value of the flux at the peak wavelength of our spectral lines. Since the wavelength binning in PyTPCI is very coarse at $\lambda/200$, we calculate this peak flux value $F_{\text{peak},\lambda}$ by assuming the integrated line area flux $F_{\text{int},\lambda}$ is what PyTPCI outputs in its continuum spectra. We then estimate the Gaussian line width σ_λ due to Doppler broadening (Eq. 9), and knowing the area of a Gaussian, we find the Gaussian's peak (Eq. 10). We use the peak flux value (the Gaussian line amplitude) and the standard deviation (the Gaussian line width) in order to construct a hypothetical Gaussian line function of wavelength versus spectral flux density, which is used for all flux calculations.

$$\sigma_\lambda = \sqrt{\frac{k_B \cdot T_{\text{outflow}}}{\mu m_H}} \cdot \frac{\lambda}{c} \tag{9}$$

$$F_{\text{peak},\lambda} = \frac{F_{\text{int},\lambda}}{\sqrt{2\pi}\sigma_\lambda} \tag{10}$$

4.2. *Instrumentation*

For each spectral line, the observability was calculated using the specifications of a well-suited telescope and instrument. For Hα, we choose KPF on Keck as a newer-generation high-resolution planetary spectrograph. For He*, we choose NIRSPEC on Keck, which has multiple confirmed absorption observations in exoplanet atmospheres for this line (Kirk et al. 2020). See Table 2 for details.

In calculations that reference an "ideal telescope", we assume a 10m diameter telescope with perfect throughput and effectively infinite resolution. See all calculated results in Table 3.

Table 2: Instrument Specifications

Line	Telescope	Instrument	Filter	Throughput (%)	Bin size
Hα	Keck	KPF	Red	10	$\lambda/343{,}000$ [a]
He*	Keck	NIRSPEC	Y-band	10	$\lambda/110{,}000$ [b]
X-ray	XMM	EPIC	Medium	90	$E/35$ [c]

[a] KPF overview.

[b] NIRSPEC filters, Y-band, high resolution, no adaptive optics. See also Zhang et al. (2022b).

[c] EPIC combined mode specifications. Medium is used in Zhang et al. (2022c).

Table 3: Outflow Calculations

System	Metallicity ($[M/H]_\odot$)	SNR Hα	Depth (ppm)	SNR He*	Depth (ppm)	Abs (%)	W (m$\AA$)	W$_{obs}$ (m$\AA$)	Bremss (nJy)	$\tau_{H\alpha}$	Peak Temperature (K)
HD 209458b	0	0.71	370	0.31	400	0.66	3.88	3.65	0.09	0.014	9,300
HD 209458b	0	0.75	400	0.61	700	1.45	9.13	–	0.19		8,800
HD 209458b	1	0.65	350	0.32	420	1.48	9.30	–	0.20	0.078	8,400
TOI-560b	100	8.4E-04	0.79	6.6E-03	14	1.24	8.53	7.76	0.01	9.1E-04	4,800
TOI-560b	0	3.6E-03	3.0	6.6E-03	12	45.40	283.00	–	0.10		4,100
WASP-69b	0	0.29	240	0.29	600	8.87	76.06	28.5	0.07		9,600
WASP-69b	0	0.46	400	0.46	960	15.60	155.78	–	0.22		9,300
WASP-69b	10	0.14	130	0.46	1020	24.28	244.74	–	0.11	0.005	6,700
WASP-107b	0	6.6E-03	83	0.13	410	34.11	508.81	100.0	0.06	0.025	8,600
WASP-107b	0	0.019	25	0.027	87	79.65	613.70	–	0.87		6,100
HD 189733b	10	0.63	210	2.4	1900	1.27	10.11	11.0	16	0.011	10,300
HD 189733b	0	1.9	610	2.2	1700	3.16	22.01	–	22		11,600
TOI-1430b	100	2.9E-04	0.27	2.1E-03	3.9	0.96	7.36	7.3	0.00	4.6E-06	4,600
TOI-1430b	0	1.5E-03	1.1	2.0E-03	3.3	16.70	92.87	–	0.03		7,900

NOTE—The bottommost data rows for simulations at 0Z were run with an illumination angle of 0° for comparison.

References—Zhang et al. (2023, Table 3)

5. OPTICAL DEPTH CALCULATIONS

CLOUDY reports the optical depth at the 912$\AA$ Lyman limit, which corresponds to the energy required to ionize a ground-state hydrogen atom. However, we are more interested in investigating the Hα optical depth, in order to find an estimate of the effective radius of our chosen systems that is less conservative than the default white-light radius. Therefore, we want to find the radius at which $\tau_{\mathrm{H}\alpha} = 1$.

We define the frequency-dependent optical depth as a function of the absorption coefficient α_ν, or equivalently, as the product of number density and interaction cross section. We want the number density of $n = 2$ hydrogen state, from which we get Hα absorption. Thus, referring to Rybicki & Lightman (1986, Eq. 1.26), we want:

$$\tau_\nu(z) = \int_{z_0}^{z} \alpha_\nu(z')dz' = \int_{1R_P}^{15R_P} n_2(z)\sigma_{H\alpha}dz' \tag{11}$$

We find the absorption coefficient using the Einstein coefficients listed on the NIST atomic spectroscopy database, calculating a spectral line strength of $S_{ij} = 1.53 \times 10^{-14}$ cm/molecule. We calculate the absorption coefficient to be $\alpha_{ij} = S_{ij} \cdot f$, where we assume f is a Gaussian line profile. Following Christie et al. (2013, Eq. 5), we can estimate the ratio of the number densities of the atoms in the $n = 1$ and $n = 2$ states as:

$$\frac{n_2}{n_1} = \frac{g_2}{g_1} \exp\left(\frac{-10.2\text{eV}}{k_B T_{\text{exc}}}\right) \tag{12}$$

With some configuration, CLOUDY can directly output the number densities of hydrogen states as a function of depth. The output excitation temperature appears nonphysically high, $T_{\text{exc}} \sim 2 \times 10^6$ K, but our outflow is certainly not in thermal equilibrium, so the excitation temperature will not be meaningful. Nonetheless, we can calculate the optical depth for Hα by integrating along the 1D radii. This conclusively shows that the line is optically thin for all systems, approaching its maximum $\tau_{H\alpha} \sim 10^{-4} - 10^{-2}$ at the lower boundary of the simulation domain $R_P = 1$. This indicates that most of the Hα emission may come from a lower, more opaque layer of the atmosphere outside of our simulation domain. Nevertheless, we are unable to choose a better radius than the white-light radius, unless we want to bound the planet by its opacity at the Lyman limit, which would be a much more radical proposition. In Table 3 we report the maximum Hα optical depth for each system.

6. BREMSSTRAHLUNG CALCULATIONS

Bremsstrahlung radiation is emitted when one charged particle is accelerated by the electric field of another. Since our outflow contains many electrons moving at appreciable velocities, we can calculate the bremsstrahlung spectrum for a thermal velocity distribution.

Following Rybicki & Lightman (1986, Ch. 5.2), we calculate the emission over a given volume and frequency as below, assuming that below the cutoff frequency, $\exp(-h\nu/k_B T) \sim 1$. We take the average charge to be $Z \approx 2$ in order to emphasize helium content, and estimate the velocity-averaged Gaunt factor as $\bar{g}_{ff} \approx 1$. Since the outflow's temperature varies with radius, it is not perfectly in thermal equilibrium, but it is a fair approximation.

$$\epsilon_\nu^{ff} = \left(6.8 \times 10^{-38} \frac{\text{ergs}}{\text{s} \cdot \text{cm}^3 \cdot \text{Hz}}\right) \cdot T^{-1/2} n_e n_i Z^2 \bar{g}_{ff} \cdot \exp\left(\frac{-h\nu}{k_B T}\right) \tag{13}$$

We integrate over a spherical volume and calculate the resultant spectral flux density in nanoJanskys. The results are shown in Table 3.

We investigate the feasibility of observing this bremsstrahlung using the upcoming Next Generation VLA (ngVLA), a new radio observatory with 10 times the spatial resolution of the current VLA, which should be able to observe between 1.2–116 GHz (C.L. Carilli 2015). Our cutoff frequency is $\nu = k_B T_{\text{outflow}}/h \sim 10^{14}$ Hz, roughly a few microns in wavelength. We require an average angular resolution of $\theta \sim 1$ mas in order to distinguish these exoplanets from their host stars. Recent technical specifications have been published by NRAO (B. Butler 2019), and ngVLA has recently uploaded an online sensitivity calculator (ngV 2024).

We could observe at a variety of radio frequencies, but we choose 8 GHz as the band that is intended to have the highest continuum sensitivity at 1 mas. We find that the best sensitivity we can theoretically reach is 1.00 μJy/beam in 1 hour on target. The maximum calculated bremsstrahlung is 0.016 μJy from HD 189733b, which is two orders of magnitude too small to be detected. The other systems have much smaller emissions than HD 189733b, and so their observability is also nil.

7. MASS LOSS CALCULATIONS

The gas outflows from these planets may be so violent that they would produce high-energy shocks, and according we attempt to estimate the mass loss rates and general properties of this outflow. We find the location of the shock by finding the point where the ram pressures of the stellar and planetary winds are equal, using mass conservation. The mass loss rate estimates $\dot{m}_{\text{est}}$ are taken from references cited in Table 4, and are compared with our own simulation estimates $\dot{m}_{\text{sim}}$.

$$\dot{m} = 4\pi r^2 \cdot \rho(r) \cdot v(r) \tag{14}$$

We approximate the stellar wind as solar, with $\rho_\odot \sim 300$ km/s and $\dot{m}_\odot \sim 1.5 \times 10^{12}$ g/s. The maximum velocity of the planetary wind varies per system, but is around 20 km/s.

Table 4: Shock Calculations

System	Metallicity	$\dot{m}_{\rm sim}$	$\dot{m}_{\rm est}$	$v_{\rm sim}$	Shock Radius
	$([M/H]_\odot)$	(g/s)	(g/s)	(km/s)	(R_P)
HD 209458b	0	5.15E+10	3.00E+10	54	24.02
TOI-560b	100	1.14E+10	2.30E+10	11	230.43
WASP-69b	0	1.00E+11	1.00E+11	55	1.49
WASP-107b	0	4.05E+11	1.00E+11	32	198.65
HD 189733b	10	5.95E+08	5.00E+09	70	32.82
TOI-1430b	100	1.07E+10	7.70E+09	10	370.63

NOTE—Each row uses the simulation most consistent with that system's observed He^* equivalent width. Wind velocity is the maximum.

References—Lampón et al. (2021), Zhang et al. (2023), Wang & Dai (2021), Kirk et al. (2020), Zhang et al. (2022a)

We show very good agreement between our simulated mass loss rates, and mass loss rates recently estimated by others in the literature. The location of the shock is extremely sensitive to the mass loss rate however, and in most cases it appears erroneously large, particularly in the cases of WASP-107b, which has a very distended atmosphere, and TOI-1430b, which does not have well-constrained mass loss measurements.

8. RESULTS

The results of our calculations do not indicate planetary outflow emissions that are currently detectable in one transit, summarized in Table 3. The planet-star flux ratio of our brightest system HD 189733b is shown in Figure 6, demonstrating that Hα and H^* emissions are the most dominant, validating our choice to focus on them. Additionally, we see prominent Na1 and Mg1 metal lines in the optical band. Our simulations also show good agreement with previous literature estimates of the mass loss rates as shown in Table 4, though all values remain unverified.

8.1. *Hydrogen-alpha*

Our results for Hα appear plausible, predicting that most SNRs will be less than 1. Hα emission was somewhat unaffected by the addition of metals into a given simulation, and consistently displayed a wide range of transit depths, with larger depths for the bigger gas giants.

8.2. *Metastable helium*

Our target young exoplanet systems all have detected absorption in metastable helium, and therefore we should also closely investigate their helium emissions. He^* emissions are definitively brighter and more significant than the emissions of any other spectral line. These SNRs are relatively weak, mostly remaining below a value of 1, though they show larger transit depths than Hα. The main exception is HD 189733b, which shows a weak but definitively present signal at SNR 2.4, with a plausible transit depth of 1900ppm (0.19%). However, this becomes a confident detection of SNR 5.4 if observed for 5 transits, which is an attainable goal for this short-period planet.

8.3. *Metal Lines and X-rays*

Adding metals to PyTPCI effectively adds X-ray emission, which is worth noting in the case of the brightest supersolar metallicity exoplanet simulated, HD 189733b. The observability of the strongest X-ray line at 6.41 keV was examined using the specifications of EPIC on XMM-Newton, yielding only SNR ~ 0.00. Nonetheless, it is useful to know that X-ray energy flux from these systems is comparable to some of the brighter lines like Hα and He^*, though the photon flux at XMM-Newton is negligible.

The observability of the line tentatively identified as Si5+Na11 in HD 189733b and TOI-1430b (see Figure 5) unfortunately remains poor. Even with an ideal telescope, for HD 189733b its SNR is below 10^{-4}.

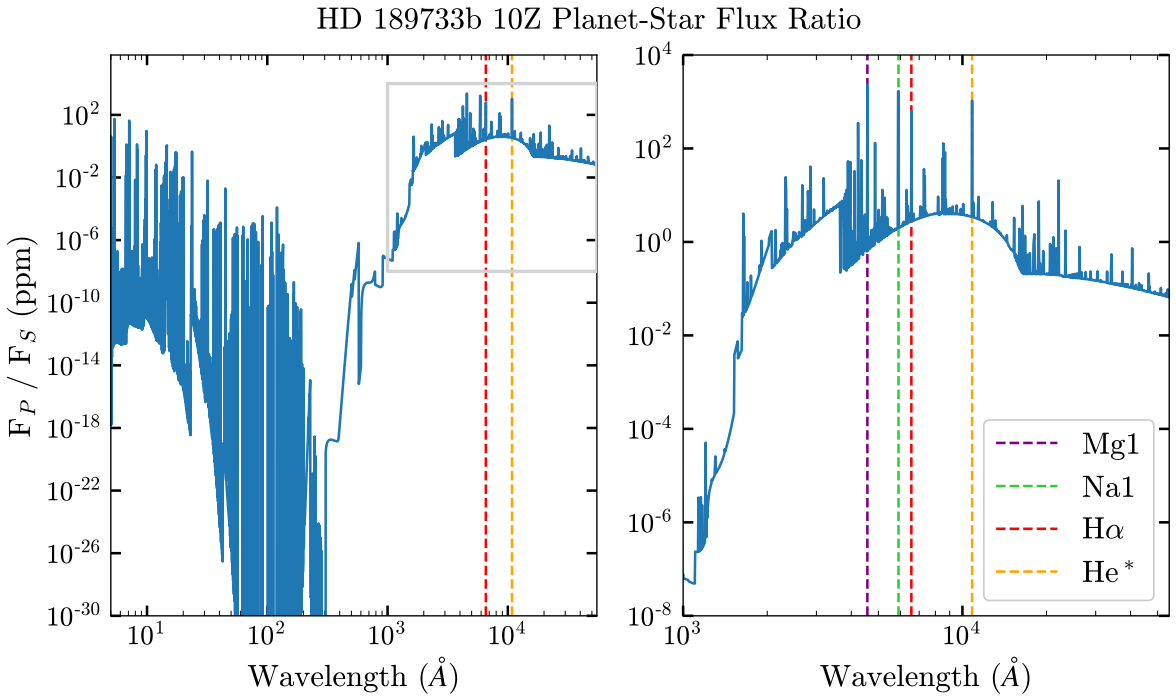

Figure 6: The planet-star flux ratio for the brightest and most promising system, HD 189733b. Note the two prominent metal lines, Na1 and Mg1.

8.4. *Comparison with Previous Literature*

We compare our results for HD 209458b 0Z and HD 189733b 0Z with the publicly-available data from Salz et al. (2016). We show strong agreement with the previous TPCI simulations run, with an acceptable amount of divergence as a result of our changes, such as implementing a kinetic temperature floor and altering the illumination angle (see Section 2.3). This indicates that our computational setup is sound, and that our improvements do notably alter simulation results. However, the zero metallicity cases are among the most simple, and likely do not completely represent reality.

The precise mechanisms of emissions in both the upper and lower atmospheres of exoplanets remain uncertain, and thus it is difficult to exhaustively describe what we might expect the planetary outflow emissions to look like. However, PLUTO and CLOUDY are both robust, generic, well-tested codes that were not built upon limited assumptions of how exoplanet outflows might behave, and thus results from PyTPCI deserve special consideration in the context of more specialized exoplanet atmosphere codes. Particularly useful is our inclusion of metals — though we did not include molecules — since the complex effects of metal cooling demonstrably affect the outflow temperature profiles, which is the key factor governing emissions. Mass loss estimates remain largely consistent with other atmosphere models, but that does not indicate anything about the truth of the mass loss rates, but only that we are at a similar place of understanding the dynamics of these outflows.

The physics of high-energy plasma and shocks of planetary outflows are even more uncertain, and so the conclusions we draw must remain constrained. However, it is reasonable to claim that one might expect significant — if currently undetectable — bremsstrahlung emissions from very hot outflows of hot Jupiters, like from HD 189733b. This holds true especially since we assume a correlation between total outflow power and planetary magnetic field strength, which shapes the outflow geometry in numerous ways beyond the scope of this paper.

9. DISCUSSION

PyTPCI has limitations, but our work has provided interesting information about the possibility of observing escaping atmosphere emissions.

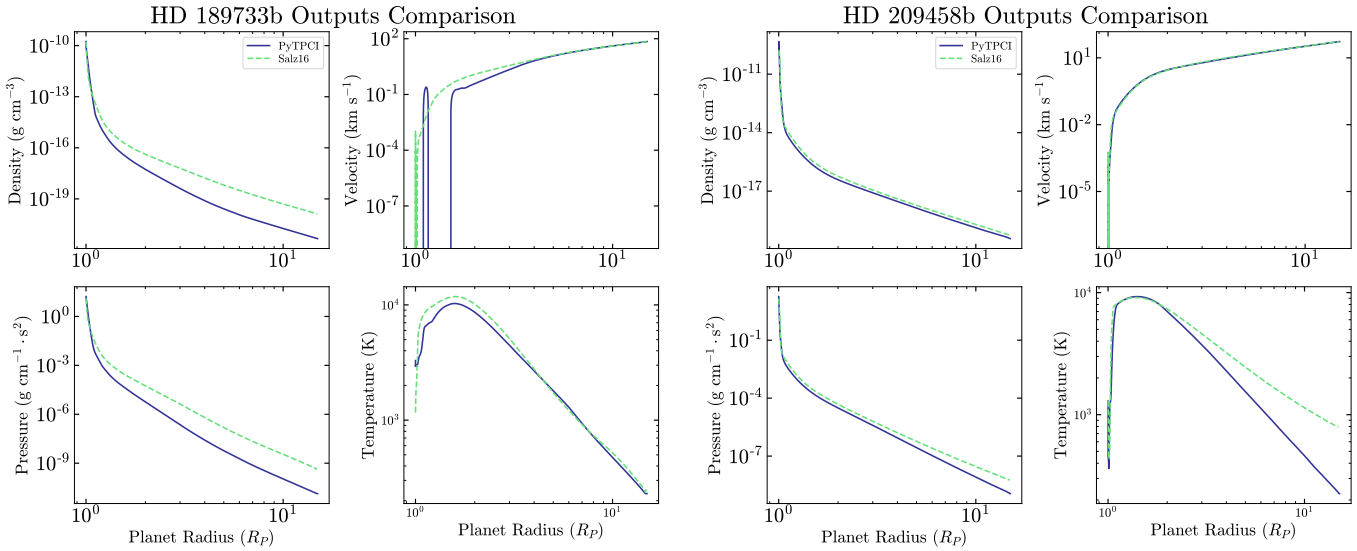

Figure 7: Our PyTPCI simulations are reasonably similar to those of Salz et al. (2016), with an expected amount of differences. A simulation of HD 189733b run with 0° illumination angle aligns perfectly (not shown).

Notably, we do not systematically take into account the effects of magnetic fields, which Adams (2011) suggests should significantly impact the outflow geometry of hot Jupiters with magnetic fields. Their theoretical model of mass outflow rate was consistent with observations of HD 209458b, but was too small for observations of HD 189733b, and further work reiterates that mass outflow rates for planets with magnetic fields should be an order of magnitude smaller than planets without (Owen & Adams 2014).

Sanz-Forcada et al. (2011) pointed out the need for more sophisticated models of stellar XUV spectra. Our constructed stellar XUV regime spectra are indeed coarse, so a better characterization of how stellar type plays into photochemical processes in atmospheres is vital, as has been further demonstrated by Locci et al. (2022).

CLOUDY has sophisticated modeling of photochemistry, but we do not have molecules enabled. Further atmospheric simulations with molecules are vital for interpreting real data (e.g. Xue et al. 2024) and predicted data (Locci et al. 2024), both of which show carbon and oxygen compounds to be significant tracers in escaping atmospheres.

There are other promising codes for evaluating escaping exoplanet atmospheres, such as EVE used in Allart, R. et al. (2019), a 3D code modeling Lyα transmission spectra in the exosphere of warm Neptune GJ 436b using a combination of analytical techniques and random Monte Carlo simulations (Bourrier et al. 2015; Bourrier, V. et al. 2016), or JADE, a code built to simultaneously simulate the orbital dynamics and photoevaporation of three-body systems using more analytical energy-limited escape equations (Attia, O. et al. 2021). ATES is another promising option: a specialized, highly-efficient 1D hydrodynamics and photoionization code that agrees very well with TPCI (Caldiroli, Andrea et al. 2021). Non-local thermodynamic equilibrium (NLTE) models are usually used for stellar atmosphere simulations, but are beginning to be used to model hot exoplanet atmospheres as well (García Muñoz & Schneider 2019; Munafò et al. 2017; Lampón et al. 2021). García Muñoz & Schneider (2019) also provides valuable insight into running hydrodynamic simulations, suggesting that it can be effective to take a converged simulation and slowly change the input conditions in order to model a different system.

Our setup neglects the effects of processes like zonal winds that can homogenize chemical compositions across the surface of a planet with drastic dayside-nightside temperature gradients, but pseudo-2D atmosphere models combining thermo- and photochemistry and fluid dynamics like Agúndez, Marcelino et al. (2014) provides a promising approach. Wang & Dai (2021) also suggest a path forward with their 3D hydrodynamics simulation of WASP-69b, which is able to coevolve hydrodynamics and thermodynamics, instead of alternately running them like PyTPCI does. That work also demonstrates the importance of including centrifugal and Coriolis forces in order to most accurately reproduce observations with models.

Though our work suggests that detecting emissions from planetary outflows is not currently feasible, there are many interesting ways forward, both with the advent of JWST and the next generation of extremely large telescopes granting superior light-gathering power, and also with the steadily-improving accuracy and complexity of computational exoplanet models.

I would like to thank Michael Zhang for his constant guidance and mentorship on this project, and Professor Jacob Bean for being the one to truly introduce me to the field of exoplanets, and for bringing me into his fantastic research group. Thank you to my secondary readers, Professor Leslie Rogers and Professor Fausto Cattaneo, for their feedback and advice. Thank you to Professor Andrey Kravtsov for his many insights into astrostatistics and the complexities of computational modeling. Thank you to Professor Malte Jansen for his advice on incorporating viscosity into fluid hydrodynamics simulations. Thank you to Professor Damiano Caprioli for his influence on the ideas of high-energy physics in this project. Many thanks to Aster Taylor for their input and suggestions on calculations, code troubleshooting, and innumerable miscellaneous things. And thank you to my friends and family for their support.

Software: TPCI (Salz et al. 2015), Cloudy 23 (Chatzikos et al. 2023), PLUTO 4.4 (Mignone et al. 2007), PHOENIX (Husser et al. 2013), CHIANTI 10 (Dere et al. 1997; Del Zanna et al. 2021)

REFERENCES

2024, Next Generation Exposure Calculation Tool. https://ngect.nrao.edu/

Adams, F. C. 2011, The Astrophysical Journal, 730, 27, doi: 10.1088/0004-637x/730/1/27

Agúndez, Marcelino, Parmentier, Vivien, Venot, Olivia, Hersant, Franck, & Selsis, Franck. 2014, AA, 564, A73, doi: 10.1051/0004-6361/201322895

Allart, R., Bourrier, V., Lovis, C., et al. 2019, AA, 623, A58, doi: 10.1051/0004-6361/201834917

Attia, O., Bourrier, V., Eggenberger, P., et al. 2021, AA, 647, A40, doi: 10.1051/0004-6361/202039452

B. Butler, W. Grammer, R. S. E. M. C. C. 2019, ngVLA Sensitivity, Tech. Rep. ngVLA Memo 21, National Radio Astronomy Observatory. https://library.nrao.edu/public/memos/ngvla/NGVLA_21.pdf

Barragán, O., Armstrong, D. J., Gandolfi, D., et al. 2022, MNRAS, 514, 1606, doi: 10.1093/mnras/stac638

Bourrier, V., Ehrenreich, D., & Lecavelier des Etangs, A. 2015, A&A, 582, A65, doi: 10.1051/0004-6361/201526894

Bourrier, V., Lecavelier des Etangs, A., Ehrenreich, D., Tanaka, Y. A., & Vidotto, A. A. 2016, AA, 591, A121, doi: 10.1051/0004-6361/201628362

Caldiroli, Andrea, Haardt, Francesco, Gallo, Elena, et al. 2021, AA, 655, A30, doi: 10.1051/0004-6361/202141497

Casasayas-Barris, N., Palle, E., Stangret, M., et al. 2021, Astronomy amp; Astrophysics, 647, A26, doi: 10.1051/0004-6361/202039539

Casasayas-Barris, N., Pallé, E., Yan, F., et al. 2018, AA, 616, A151, doi: 10.1051/0004-6361/201832963

Charbonneau, D., Brown, T. M., Latham, D. W., & Mayor, M. 2000, ApJL, 529, L45, doi: 10.1086/312457

Charbonneau, D., Brown, T. M., Noyes, R. W., & Gilliland, R. L. 2002, ApJ, 568, 377, doi: 10.1086/338770

Chatzikos, M., Bianchi, S., Camilloni, F., et al. 2023, RMxAA, 59, 327, doi: 10.22201/ia.01851101p.2023.59.02.12

Christie, D., Arras, P., & Li, Z.-Y. 2013, The Astrophysical Journal, 772, 144, doi: 10.1088/0004-637x/772/2/144

C.L. Carilli, M. McKinnon, J. O. A. B. A. I. E. M. A. L. C. C. A. M. M. L. J. H. G. B. P. D. C. H. M. H. J. d. F. D. N. B. K. B. C. B. B. 2015, Science Working Groups: Project Overview, Tech. Rep. ngVLA Memo 5, National Radio Astronomy Observatory. https://library.nrao.edu/public/memos/ngvla/NGVLA_05.pdf

Czesla, S., Lampón, M., Sanz-Forcada, J., et al. 2022, AA, 657, A6, doi: 10.1051/0004-6361/202039919

Del Zanna, G., Dere, K. P., Young, P. R., & Landi, E. 2021, ApJ, 909, 38, doi: 10.3847/1538-4357/abd8ce

Dere, K. P., Landi, E., Mason, H. E., Monsignori Fossi, B. C., & Young, P. R. 1997, A&AS, 125, 149, doi: 10.1051/aas:1997368

Diemer, B. 2022, ASTRO 670: Hydrodynamics. http://www.benediktdiemer.com/wp-content/uploads/astr670_hydro_notes.pdf

García Muñoz, A., & Schneider, P. C. 2019, ApJL, 884, L43, doi: 10.3847/2041-8213/ab498d

Harada, C. K., Kempton, E. M. R., Rauscher, E., et al. 2021, ApJ, 909, 85, doi: 10.3847/1538-4357/abdc22

Husser, T.-O., Wende-von Berg, S., Dreizler, S., et al. 2013, Astronomy amp; Astrophysics, 553, A6, doi: 10.1051/0004-6361/201219058

Jensen, A. G., Redfield, S., Endl, M., et al. 2012, The Astrophysical Journal, 751, 86, doi: 10.1088/0004-637X/751/2/86

Johnstone, C. P., Güdel, M., Lammer, H., & Kislyakova, K. G. 2018, Astronomy amp; Astrophysics, 617, A107, doi: 10.1051/0004-6361/201832776

Kirk, J., Alam, M. K., López-Morales, M., & Zeng, L. 2020, The Astronomical Journal, 159, 115, doi: 10.3847/1538-3881/ab6e66

Lampón, M., López-Puertas, M., Czesla, S., et al. 2021, A&A, 648, L7, doi: 10.1051/0004-6361/202140423

Lampón, M., López-Puertas, M., Sanz-Forcada, J., et al. 2021, Astronomy amp; Astrophysics, 647, A129, doi: 10.1051/0004-6361/202039417

Linsky, J. L., Wood, B. E., Youngblood, A., et al. 2020, The Astrophysical Journal, 902, 3, doi: 10.3847/1538-4357/abb36f

Locci, D., Aresu, G., Petralia, A., et al. 2024

Locci, D., Petralia, A., Micela, G., et al. 2022, PSJ, 3, 1, doi: 10.3847/PSJ/ac3f3c

Malsky, I., Rauscher, E., Roman, M. T., et al. 2024, The Astrophysical Journal, 961, 66, doi: 10.3847/1538-4357/ad0b70

Mignone, A., Bodo, G., Massaglia, S., et al. 2007, ApJS, 170, 228, doi: 10.1086/513316

Munafò, A., Mansour, N. N., & Panesi, M. 2017, The Astrophysical Journal, 838, 126, doi: 10.3847/1538-4357/aa602e

Nortmann, L., Pallé, E., Salz, M., et al. 2018, Science, 362, 1388, doi: 10.1126/science.aat5348

Oklopčić, A. 2019, ApJ, 881, 133, doi: 10.3847/1538-4357/ab2f7f

Oklopčić, A., & Hirata, C. M. 2018, ApJL, 855, L11, doi: 10.3847/2041-8213/aaada9

Owen, J. E., & Adams, F. C. 2014, Monthly Notices of the Royal Astronomical Society, 444, 3761–3779, doi: 10.1093/mnras/stu1684

Perryman, M. 2018, The Exoplanet Handbook, 2nd edn. (Cambridge University Press)

Raymond, J. C., & Smith, B. W. 1977, ApJS, 35, 419, doi: 10.1086/190486

Rybicki, G. B., & Lightman, A. P. 1986, Radiative Processes in Astrophysics

Salz, M., Banerjee, R., Mignone, A., et al. 2015, Astronomy amp; Astrophysics, 576, A21, doi: 10.1051/0004-6361/201424330

Salz, M., Czesla, S., Schneider, P. C., & Schmitt, J. H. M. M. 2016, A&A, 586, A75, doi: 10.1051/0004-6361/201526109

Salz, M., Czesla, S., Schneider, P. C., et al. 2018, AA, 620, A97, doi: 10.1051/0004-6361/201833694

Sanz-Forcada, J., Micela, G., Ribas, I., et al. 2011, A&A, 532, A6, doi: 10.1051/0004-6361/201116594

Seager, S., & Sasselov, D. D. 2000, ApJ, 537, 916, doi: 10.1086/309088

Snellen, I. A. G., Albrecht, S., de Mooij, E. J. W., & Le Poole, R. S. 2008, A&A, 487, 357, doi: 10.1051/0004-6361:200809762

Spake, J. J., Sing, D. K., Evans, T. M., et al. 2018, Nature, 557, 68, doi: 10.1038/s41586-018-0067-5

Vidal-Madjar, A., Lecavelier des Etangs, A., Désert, J. M., et al. 2003, Nature, 422, 143, doi: 10.1038/nature01448

Vissapragada, S., Knutson, H. A., Jovanovic, N., et al. 2020, The Astronomical Journal, 159, 278, doi: 10.3847/1538-3881/ab8e34

Wang, L., & Dai, F. 2021, ApJ, 914, 98, doi: 10.3847/1538-4357/abf1ee

Winn, J. N. 2014, Transits and Occultations. https://arxiv.org/abs/1001.2010

Wood, B. E., Redfield, S., Linsky, J. L., Müller, H.-R., & Zank, G. P. 2005, ApJS, 159, 118, doi: 10.1086/430523

Woods, T. N., & Rottman, G. J. 2002, Geophysical Monograph Series, 130, 221, doi: 10.1029/130GM14

Xue, Q., Bean, J. L., Zhang, M., et al. 2024, The Astrophysical Journal Letters, 963, L5, doi: 10.3847/2041-8213/ad2682

Zhang, M., Cauley, P. W., Knutson, H. A., et al. 2022a, The Astronomical Journal, 164, 237, doi: 10.3847/1538-3881/ac9675

Zhang, M., Dai, F., Bean, J. L., Knutson, H. A., & Rescigno, F. 2023, ApJL, 953, L25, doi: 10.3847/2041-8213/aced51

Zhang, M., Knutson, H. A., Dai, F., et al. 2023, The Astronomical Journal, 165, 62, doi: 10.3847/1538-3881/aca75b

Zhang, M., Knutson, H. A., Wang, L., Dai, F., & Barragán, O. 2022b, The Astronomical Journal, 163, 67, doi: 10.3847/1538-3881/ac3fa7

Zhang, M., Knutson, H. A., Wang, L., et al. 2022c, The Astronomical Journal, 163, 68, doi: 10.3847/1538-3881/ac3f3b